Geochemistry, Geophysics, Geosystems®

AGU ADVANCING EARTH AND SPACE SCIENCES

RESEARCH ARTICLE
10.1029/2023GC011018

Key Points:

- Parent magma silica content influences the median 2D shape of an igneous zircon population
- Major controls of median zircon 2D boundary shape appear extrinsic to the crystal
- Predominant zircon crystallization processes differ between mafic and felsic rocks

Supporting Information:

Supporting Information may be found in the online version of this article.

Correspondence to:

T. Scharf,
t.scharf@postgrad.curtin.edu.au

Citation:

Scharf, T., Kirkland, C. L., Barham, M., Yakymchuk, C., & Puzyrev, V. (2023). Does zircon shape retain petrogenetic information? *Geochemistry, Geophysics, Geosystems*, *24*, e2023GC011018. https://doi.org/10.1029/2023GC011018

Received 24 APR 2023
Accepted 10 AUG 2023

Author Contributions:

Conceptualization: C. L. Kirkland
Data curation: T. Scharf
Formal analysis: T. Scharf, C. Yakymchuk
Funding acquisition: M. Barham
Investigation: T. Scharf
Methodology: T. Scharf
Project Administration: M. Barham
Resources: C. L. Kirkland
Supervision: C. L. Kirkland, M. Barham, V. Puzyrev
Writing – original draft: T. Scharf, C. L. Kirkland, M. Barham, C. Yakymchuk, V. Puzyrev

Does Zircon Shape Retain Petrogenetic Information?

T. Scharf[1], C. L. Kirkland[1], M. Barham[1], C. Yakymchuk[2], and V. Puzyrev[1,3]

[1]Timescales of Mineral Systems Group, School of Earth and Planetary Sciences, Curtin University, Perth, WA, Australia, [2]School of Earth and Environmental Sciences, University of Waterloo, Waterloo, ON, Canada, [3]Curtin Centre for Optimisation and Decision Science, School of Electrical Engineering, Computing and Mathematical Sciences, Curtin University, Perth, WA, Australia

Abstract Zircon shape is commonly reported during geochronology and geochemistry analyses of igneous, metamorphic, and sedimentary rocks, but the relationship of zircon shape to primary growth environmental conditions remains poorly constrained. Current models for the control on igneous zircon shape focus on the relative growth of crystal prisms and pyramids, which are not discernible in the imaging techniques used for rapid quantification of zircon shape in geochronology sample mounts. We model the relationship between whole-rock composition and zircon 2D shape in mineral separates from 45 mafic to felsic igneous samples, representative of Archean and Proterozoic crust in Western Australia. Shape parameters are derived from semi-automated measurement of photomicrographs of polished zircon crystals in epoxy resin mounts. Whole-rock composition shows a statistically significant relationship to median magmatic zircon crystal area and mathematically defined "roundness." Zircon populations show reduced median area and increased median roundness as whole-rock silica decreases. Phase equilibrium modeling based on whole-rock composition, and automated electron microscopy mineral maps, indicates that the compositional predisposition of zircon shape is influenced by fundamentally different physical growth environments in mafic versus felsic melts. Specifically, influential factors that differ between mafic and felsic liquids include crystallization sequence and duration—which influence unconstrained growth space—and the potential for absorption/exsolution of zirconium from the accompanying mineral assemblage. We present quantitative, explanatory models for the relationship between zircon 2D shape and whole-rock silica and demonstrate that the relationships are adhered to across a broad spectrum of whole-rock compositions.

Plain Language Summary Zircon is a resilient mineral that can preserve chemical information over billions of years and is used to date different types of rocks. The 2D boundary shapes of polished zircon crystals are commonly reported during their analysis. However, it is challenging to interpret the geological meaning of the 2D shapes as little is known about how the crystals' growth environment affects them. Current understanding is mostly based on 3D crystal faces that are not easily interpreted from imaging techniques geared toward rapid measurements of large quantities of zircon grains, as used during typical isotopic analysis of this mineral. We investigate whether there is geological information in easily acquired 2D zircon boundary shape. We measured the 2D shapes of zircons from different rock types and model how the shape changes with rock composition. We then model how different rock types crystallize and compare the crystallization models to mineral growth relationships seen in the rocks. We find that the 2D shape of zircon is affected by growth space, growth duration, and competition for mineral components. These three factors vary with rock composition. Thus, zircon 2D shape varies with rock composition, hinting at potentially useful, currently untapped, additional information stored in zircon grains.

1. Introduction

Zircon is one of the most important minerals for geochronology (Hanchar, 2013; Hoskin & Schaltegger, 2003), yet the information stored in its grain shape is poorly understood. It is a priori knowledge that a magmatic body produces a population of zircon crystals with similar physical characteristics (Poldervaart, 1956). Despite this, zircon shape analysis has been hindered by a limited understanding of the fundamental controls on zircon grain shape (Zeh & Cabral, 2021). Here, we investigate the relationships between magma composition and zircon 2D boundary shape. We consider whether these relationships are discernible across a broad range of zircon source rock compositions and link these relationships to petrographic processes.

Understanding magmatic controls on crystal development has long been used to qualitatively interpret magmatic histories from the distributions of igneous mineral shapes and sizes (e.g., Cashman & Marsh, 1988; Higgins, 2000; Mangler et al., 2022; Marsh, 1988). Although parent melt physico-chemical conditions have been known to influence zircon crystal shape for decades (Larsen & Poldervaart, 1957), the nature of the composition-to-shape relationships are in essence qualitative, with a focus on higher silica rock types that have higher zircon yields (Moecher & Samson, 2006). Previous models on the controls of zircon crystal growth have assessed the relative development of crystal pyramids and prisms under instantaneous magmatic conditions (e.g., Benisek & Finger, 1993; Pupin, 1980; Vavra, 1990). The development of zircon prisms, pyramids, and elongation has been variously ascribed to the composition and temperature of the melt, melt kinetics, and crystallization rates (Benisek & Finger, 1993; Ribbe, 1982). For example, Pupin (1980) concluded that agpaicity (ratio of Na + K to Al) and temperature would independently influence the development of zircon pyramids and prisms, respectively. Vavra (1990) assigned the control on prism development to $ZrSiO_2$ saturation, and that of pyramid development to the adsorption of foreign elements onto crystal faces. Benisek and Finger (1993) attributed the control of prisms to the concentration of U and Y(REE)PO_4 in the melt. Furthermore, crystal elongation has been correlated with crystallization rate (Corfu et al., 2003; Kostov, 1973).

Zircon is a highly durable mineral, able to endure multiple geological events (Hanchar, 2013). Consequently, zircon xenocrysts can be common in igneous rocks (e.g., GSWA, 2019). Zircon has recently been shown to even persist through solid phase transfer in subduction settings (Aitchison et al., 2022) and survive long residence times in the mantle (Cambeses et al., 2023). It can be challenging to identify similarly aged xenocrysts, particularly if their textures and compositions are comparable to those of primary magmatic crystals (Erdmann et al., 2010). In Zr-undersaturated melts that lack primary zircon, inherited zircon may be misinterpreted as neocrystic zircon (Olierook et al., 2020). Zircon 2D morphology is a potential discriminant that may facilitate the discernment of primary and inherited zircon populations in an igneous rock. It would thus be advantageous to better understand how the shape of zircon crystals relates to the composition of the primary magma. The importance of zircon shape persists in a sedimentary setting, as the partial preservation of igneous zircon 2D shape parameters between source and sediment has been demonstrated (Markwitz & Kirkland, 2018). Similarities between detrital and igneous zircon 2D shapes have aided the identification of sediment sources, when used in conjunction with isotopic data (Gartmair et al., 2023; Makuluni et al., 2019).

In the case of both igneous and detrital zircon, knowledge of the controls on zircon 2D shape would improve geological interpretations. However, there is a fundamental knowledge gap between what we know of the controls on zircon shape (i.e., relative growth of prisms and pyramids under various magmatic conditions) and the way in which we presently characterize and report zircon shape in modern geochronology studies (i.e., shape parameters derived from grain boundaries in 2D). Crystal face information is not accessible in studies where zircon shape is measured from the 2D boundaries of zircon images, as these images do not capture individual crystal face information. Moreover, different configurations of zircon prisms and pyramids may give rise to similar 2D boundaries, and thus be indistinguishable in terms of their 2D shape measurements (Figure S1 in Supporting Information S1). We thus need to consider the relationship between igneous zircon 2D shape and source rock composition. In this work, we investigate whether a link between igneous 2D zircon shape and source rock composition is discernible in a typical zircon separate prepared for geochronology and across a broad range of magma compositions (mafic to felsic). We further consider the petrographic processes responsible for these links.

2. Methods

The Geological Survey of Western Australia (GSWA) maintains a state-wide public repository of geochronology (DMIRS, 2022b) and geochemistry (DMIRS, 2022a) spanning four billion years of Earth history in Western Australia (Text S3.1 in Supporting Information S1). From these repositories, we use 45 previously dated zircon separates sourced from magmatic parent rocks with distinct compositions (47%–74% SiO_2) and crystallization ages (3,315–134 Ma) (Figure 1). The broad spread of ages and whole-rock chemistries are reflective of Proterozoic to Archean continental crust (Figure S2 in Supporting Information S1). With this data set, we analyze the relationships between igneous zircon crystal shape and whole-rock composition.

Published geochronology reports (GSWA, 2019) interpret each zircon analysis as an age of igneous crystallization, xenocryst formation, or metamorphism and determine whether the data are concordant or subject to secondary processes such as radiogenic-lead loss. Zircon grains identified as having xenocrystic components or otherwise

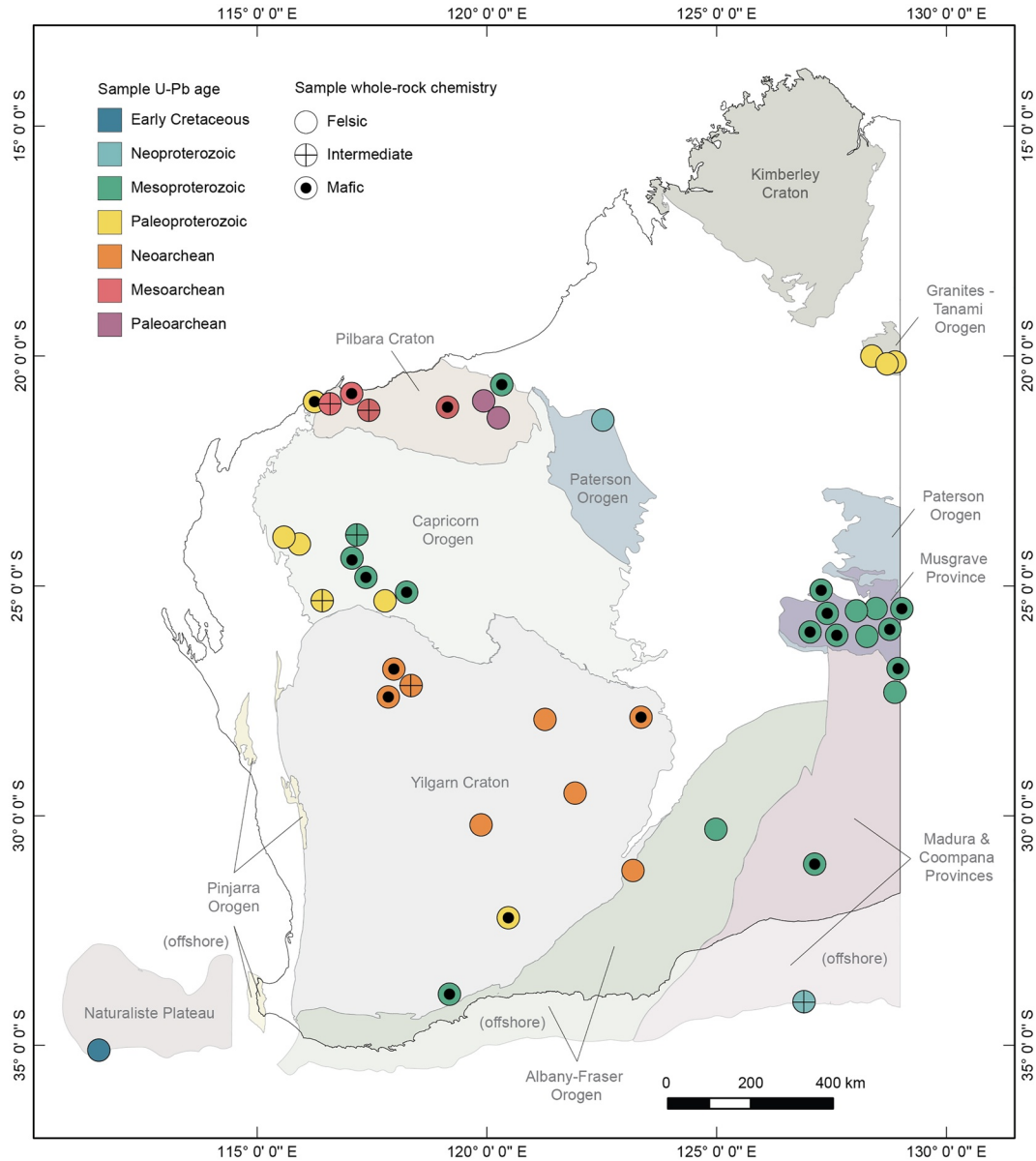

Figure 1. Schematic representation of the spatial, temporal and compositional distribution of samples used in this study, overlain on relevant generalized crustal units of Western Australia. No sedimentary basins are shown. Sample points have been dispersed to avoid overlap and aid visualization. Samples are thus slightly displaced from their true coordinates.

identified as non-igneous (e.g., metamorphic, discordant, or subject to secondary processes) were excluded from further measurement to enable the data set to directly address relationships between whole-rock composition and primary igneous zircon grain shape. The ratio of xenocrysts to primary igneous zircon was calculated for each sample (Data Set S1). Discordant analyses were excluded from the calculation. Those samples containing greater than 5% xenocrysts were visually inspected to determine whether any of the undated zircon present in the mount images displayed visual characteristics indicative of inherited zircon components in cathodoluminescence (CL), reflected light (RL), or transmitted light (TL) images. For example, xenocrysts may display colors, shapes, or internal textures that are distinct from the igneous zircon component in the sample. Potential xenocrysts were removed from the data set. On rare occasions when a grain had multiple analyses interpreted to represent igneous crystallization age, the analysis with the smallest analytical uncertainty was selected to represent the grain. A threshold of 1.5 Ga was used to select between $^{238}U/^{206}Pb$ (younger) and $^{207}Pb/^{206}Pb$ (older) isotope ratios for age determination (Spencer et al., 2016).

The zircon shape data set comprised 7,199 crystals from the 45 samples (Data Set S1), whose shapes were measured from binary (black and white) images constructed from combined RL and TL images using AnalyZr (Scharf et al., 2022). AnalyZr automatically overlays the results of binarizing both the RL and TL images, to create a combined image that represents both the exposed zircon visible in an RL image and the zircon margin (if any) visible below the resin in a TL image (e.g., Figure S3 in Supporting Information S1). This ensures a more accurate 2D grain shape, as the use of RL images alone can underestimate grain size when grain margins are obscured by resin (Scharf et al., 2022; Sitar & Leary, 2022). AnalyZr automatically excludes any grains in contact with the image boundary, as these do not have their full shape exposed for measurement. Unwanted objects (e.g., non-zircon grains, xenocryst zircons) were manually flagged for removal in the AnalyZr system. Zircon grains that appear fragmented remained in the samples and were measured alongside full zircon crystals for two reasons: (a) to test the results of shape measurement on a typical zircon separate used in geochronology and (b) zircon has been shown to have natural irregular shapes that can be misidentified as broken fragments (Larsen & Poldervaart, 1957). Stereological corrections of zircon size were not applied to the data obtained from the hand-picked zircon mounts, since on average per mount, crystals were polished to half-grain thickness producing grain boundaries comparable to projected grain outlines (Higgins, 1994).

Thirteen shape parameters are output by AnalyZr (Text S3.2, Figure S4 in Supporting Information S1); however, several of the shape parameters are mathematically related and thus capture correlated information. To reduce the shape measurement data set and identify the parameters most descriptive of zircon grain shape, a nonparametric correlation matrix and hierarchical clustering dendrogram were produced using SPSS (IBM Corp., 2020). Five clusters of shape parameters were identified: areas, lengths, aspect ratio, roundness, and form factor (Figure S5 in Supporting Information S1). Cluster analysis identified area as a prominent zircon shape descriptor. Shape descriptors in the "lengths" cluster were closely correlated to zircon area, and thus not considered further. Roundness is a prominent shape descriptor with low correlation to area and an easily comprehended shape definition. Here roundness refers to the relationship between the zircon 2D area and major axis, as defined in Text S3.2 in Supporting Information S1. Zircon area and roundness were thus selected to describe zircon grain shape in this study. Area and roundness demonstrate a subtle inverse correlation such that smaller zircon area trends toward higher zircon roundness, when considering median values per sample (Figure S6 in Supporting Information S1). No strong relationship is discernible on a grain-by-grain basis using linear regression.

Zircon grain shape measurements were thereafter aggregated to determine median shape measurements for each sample. The aggregated shape data set comprises 45 data points (samples) for each shape parameter. Shape measurements were integrated with published whole-rock composition data sets (DMIRS, 2022a). Where the same element was analyzed in multiple batches and/or using multiple techniques, the measurement with the smallest reported uncertainty was selected for further analysis.

Nonparametric correlations using Spearman's Rho were used to identify potentially meaningful relationships between whole-rock composition and median zircon area and roundness at the sample level. Spearman's Rho is one of the most commonly used nonparametric estimators in the scientific literature, advantageous for small data sets with weaker *p*-values (Xu et al., 2013). The strongest correlations were selected for further consideration, provided the number of samples used in the correlation was not less than 36 (80% of the data set). In addition to the major and minor trace element data, the parameter M defined as $(Na + K + 2Ca)/(Al \times Si)$ was considered. M provides a proxy for the chemical mechanisms by which zircon is dissolved in a melt (Boehnke et al., 2013). M is a cation ratio descriptive of the melt composition, used in zircon solubility equations, as zircon's solubility increases with increasing $(Na + K)/Al$ and Ca and decreasing SiO_2 (Watson & Harrison, 1983).

The whole-rock silica-to-shape correlations identified as potentially meaningful were quantitatively modeled using linear regression. We elect to use Ordinary Least Squares regression over more computationally powerful regression approaches such as neural networks, a form of machine learning. While neural networks have been used to build highly accurate predictive models in many fields, the scientific meaning of the resultant models can be difficult to interpret (McGovern et al., 2019; Toms et al., 2020). The well-understood underlying statistical models and associated metrics of Ordinary Least Squares linear regression provide comparatively greater transparency for the assessment of the nature of these relationships and interpreting the physical processes in operation. Linear regression was performed in Minitab (Minitab, Inc., 2022).

Composition-to-shape regression models are placed in the context of magmatic evolution by means of phase equilibrium models that predict zircon growth from melt in a closed-system, assuming equilibrium conditions

(Text S3.3 in Supporting Information S1). The models were generated for felsic samples 88411 and 190228, and mafic samples 143445 and 194762. Samples 88411 and 143445 have zircon shape measurements that are typical for the felsic and mafic data subsets, respectively. They are thus used to compare the magmatic evolution of end member melt types. Samples 190228 and 194762 are high temperature, dry melts from the Musgrave Province, Western Australia (Figure 1).

Tescan integrated mineral analyzer (TIMA) classification data were used to identify surrounding minerals and growth textures. These data were used to interpret aspects of zircon's physical growth environment that may have influenced crystal boundary shape in mafic and felsic rocks (Text S3.4 in Supporting Information S1). Rock billets (cut rock measuring 3 × 45 × 25 mm) were analyzed for GSWA samples 194793 (monzogranite, 74.3% SiO_2), 189563 (syenogranite, 73.0% SiO_2), 190228 (granite, 67.5% SiO_2), 194762 (leucogabbro, 46.6% SiO_2), and 194763 (gabbro, 48.0% SiO_2), all of which are part of the shape data set, and two of which were used for phase equilibrium modeling.

Zircon mineral associations obtained from TIMA mineral maps, and growth textures obtained from back-scattered electron (BSE) images, were compared across the size spectrum of zircon in each sample. The dimensions of the billets precluded the use of micro-CT for 3D characterization of zircon grains. Size populations were approximated from 2D TIMA images. The polished billet surface presents randomly oriented intersections through in situ zircon crystals, which do not present true zircon lengths (Higgins, 1994). Cumulative frequency plots of zircon intersection length were created for each sample, using the Freedman-Diaconis rule (Freedman & Diaconis, 1981) to determine bin width and count to best represent the data of each sample. All plots show two inflection points at approximately the 70th and 95th percentiles. Zircon intersection lengths were divided into three groups: 1st–70th, 70–95th, and 95–100th percentiles, for each sample. As intersection lengths present reduced zircon lengths, the 95–100th percentile group will contain intersections with the largest zircon. The 1–70th percentile group will contain the smallest zircons, as well as intersections with larger zircon. The 70–95th percentile includes intersections with zircon of various size fractions, excluding the smallest.

To determine whether the growth relationships seen in TIMA billet data are applicable to the hand-picked zircon populations of the GSWA mounts, the distributions of the two zircon shape data sets were compared. Zircon typically has an elongated form factor and tends to lie along its long axis when placed in mounts. As the zircon grains are preferentially aligned along their long-axis and polished to half-grain thickness, no stereographic projection of the shapes was applied to zircon in mounts. To facilitate the analysis of zircon shape in billets, the distribution of zircon long and short axes in 3D (crystal size distribution—CSD) were modeled for each billet. Zircon CSD's were derived from long and short axis measurements of TIMA 2D zircon intersections, using ShapeCalc (Mangler et al., 2022) to model the likely 3D zircon shape, and CSDCorrections (Higgins, 2000) to model long and short axis distributions. CSD modeling accounted for rock fabric using TIMA measured orientations of zircon intersections.

3. Results

3.1. Geochemistry

Using silica as an indicator of the mafic/felsic nature of a rock, we consider general trends in zircon shape with changing whole-rock silica. Individual zircon grains (Data Set S1) were binned according to whole-rock silica, and the median shape measurement calculated for each silica bin. Bin medians follow the trend of the population distribution, whilst reducing the effect of outliers. Median area increases from the 45%–50% SiO_2 bin to the 60%–65% bin, but decreases above 65% (Figure 2a). A similar pattern occurs in major and minor axis lengths but is most pronounced in the major axis length (R^2 = 88%, Figure 2c). Median zircon crystal roundness decreases from low to high silica compositions but increases at silica content above 65% (Figure 2d). There thus appears to be three shape regimes: low silica (<55%), intermediate-felsic (55%–65%), and high silica (≥65%). In this data set, the least round zircon occurs in the 60%–65% silica bin, which also corresponds to the largest zircon. Zircon from the 70%–75% bin presents similarly to that of the 55%–60% bin.

Correlations of whole-rock geochemistry with zircon median area and roundness at the sample level are provided in Table S2 in Supporting Information S1 and summarized in Figure 3. *P*-values provide a means to assess the strength of evidence against the null hypothesis of Spearman's correlation, namely, that there is no monotonic relationship between the correlates. It is common practice to interpret those correlations with *p*-values below 0.05

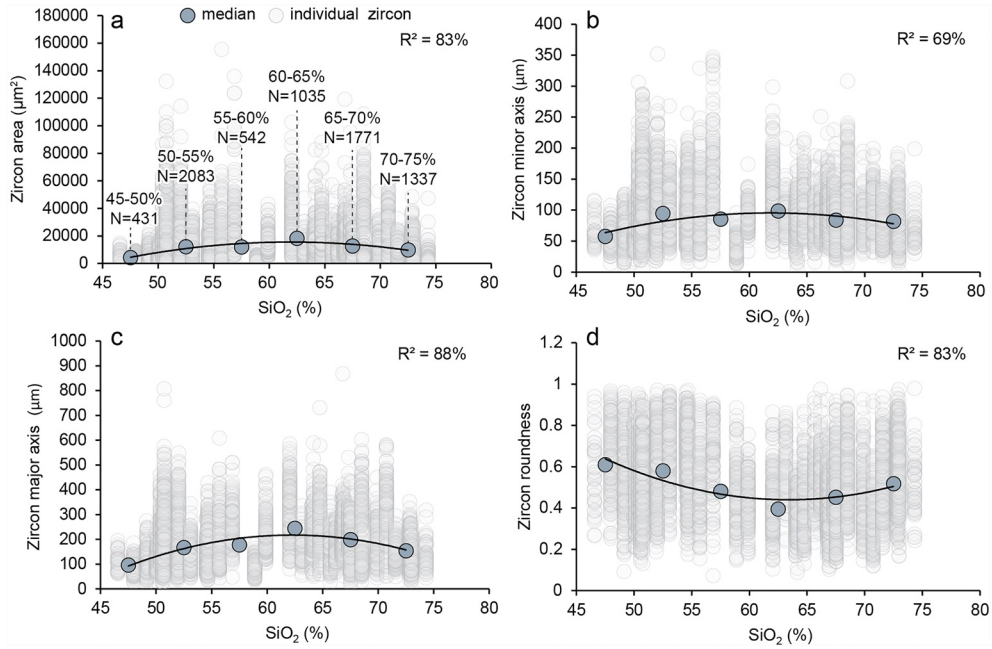

Figure 2. Biplots show the change in zircon area, roundness, major axis length and minor axis length with changing whole-rock silica across six silica bins: 45%–50%, 50%–55%, 55%–60%, 60%–65%, 65%–70%, 70%–75%. Gray data points show individual zircon measurements (7,199 grains), blue data points show the median measurements for silica bins. Bin ranges and zircon count per bin are provided in inset (a). Regression lines model the relationship between the bin median shape measurements and SiO_2 (%). The strength of the relationship is indicated by R^2. (a) Area vs. SiO_2. (b) Minor axis vs. SiO_2. (c) Major axis vs. SiO_2. (d) Roundness versus SiO_2.

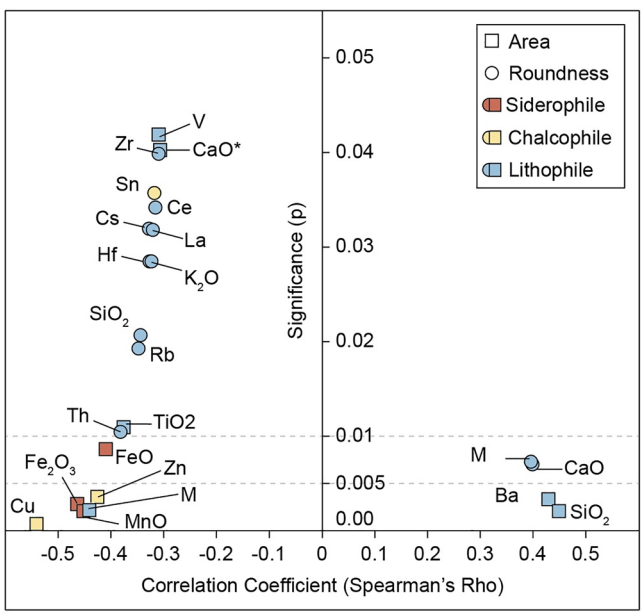

Figure 3. Summary of the chemical parameters that correlate with sample median zircon area and roundness. All chemical parameters plotted show correlations with 2-tailed *p*-values at or below 0.05. Dashed lines indicate the 0.01 and 0.005 significance levels. All chemical parameters plotted have an N above 36 and are thus based on greater than 80% of the aggregated shape data set. M = (Na + K +2Ca)/(Al × Si). Correlation coefficients, 95% confidence limits, and sample counts are tabulated in Table S2 in Supporting Information S1.

as sufficient to dismiss the null hypothesis. However, a significance level of 0.05 is not universally suitable and may not be sufficiently rigorous as it presents a high false positive risk (Benjamin & Berger, 2019; Benjamin et al., 2018; Colquhoun, 2014). Some advocate for the use of p-values as low as 0.005 due to a lower false positive risk, while considering p-values of 0.005–0.05 as "statistically suggestive" to reduce the false negative risk (Benjamin et al., 2018). We thus present all correlations with $p < 0.05$ and indicate those correlations at a significance level of 0.01 and 0.005, in Table S2 in Supporting Information S1 and Figure 3. We also include the correlation coefficient 95% lower and upper confidence limits in Table S2 in Supporting Information S1. Where the 95% confidence interval overlaps zero (e.g., Ni in Table S2 in Supporting Information S1), there is reasonable chance that no correlation exists between the shape parameter and composition; thus, the sample results are disregarded.

The whole-rock compositional elements that correlate with zircon shape form two distinct groups: sample median area correlates and median roundness correlates (Figure 3). Area shows positive correlations with indicators of felsic melt, such as SiO_2 and Ba, and negative correlations with mafic components for example, Ca, siderophile and chalcophile metals. Area is also inversely related to zircon solubility, as indicated by the negative correlation with M. The behavior of sample median roundness is opposite to that of median area. Roundness shows positive correlations with indicators of a mafic melt, M and Ca, but inverse correlations with indicators of a felsic melt, SiO_2 and rare earth elements. Ranking the strength of correlation by p-value and thereafter by correlation coefficient, we find that Cu > Mno ≈ SiO_2 for sample median area and CaO ≈ M > Th > Rb > SiO_2 for sample median

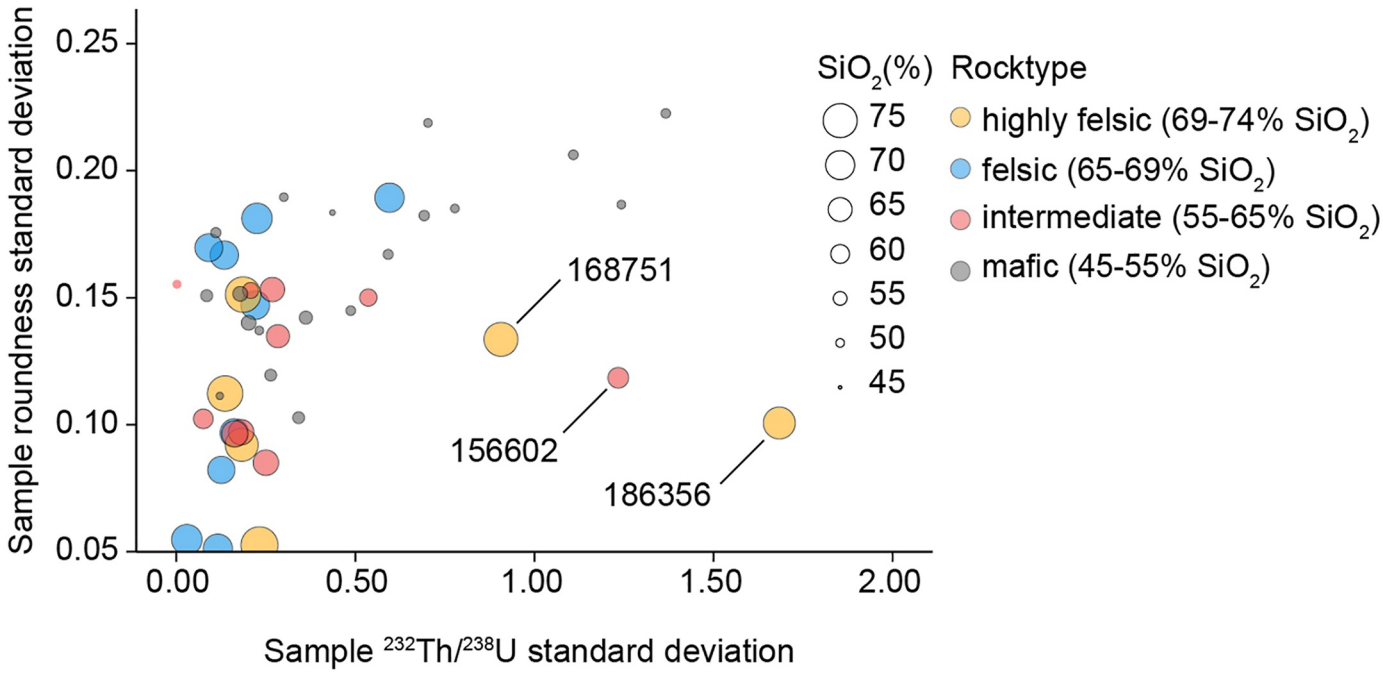

Data	Corr. Coeff	95% lower	95% upper	p
<55% SiO_2	0.626	0.240	0.841	0.003
≥55% SiO_2*	0.361	-0.097	0.693	0.108

*Excludes 156602, 168751, 186356

Figure 4. Biplot of standard deviation in zircon roundness versus standard deviation in zircon Th/U, per sample. A moderate positive correlation (0.63 correlation coefficient) of potential significance ($p < 0.005$) exists in the low silica samples (<55% SiO_2). No strong evidence of a correlation exists in samples of higher silica content.

roundness. Regression models of these relationships demonstrate that SiO_2 provides the best fit regression model for median area, while CaO provides the best-fit model for median roundness, followed by SiO_2 and M (Figure S7 in Supporting Information S1).

P, Y, Ti, heavy rare earth elements, U, Th, Ce, Nb, and Ta are all known to preferentially partition into zircon in granitic melts (Belousova et al., 2002; Hanchar, 2013; Hanchar & van Westrenen, 2007; Hoskin & Schaltegger, 2003; Nardi et al., 2013; Rubatto, 2002; Schulz et al., 2006; Tailby et al., 2011). The concentration of these chemical species at the whole-rock level shows weak to no correlation with median sample zircon area and roundness. For example, whole-rock U, Eu, and Y show no statistically significant relationship to either area or roundness and do not feature in Figure 3, while Zr is only correlated to roundness and returns one of the weakest p-values.

It has been suggested that the incorporation of U into the zircon crystal lattice may impact zircon major axis length (Makuluni et al., 2019). Although trace element composition is not available for the full GSWA geochronology data set, U (ppm) and Th (ppm) concentrations are available for dated grains in each sample. Across the full data set, we find an apparent linear correlation between grain U and grain roundness; however, this is driven entirely by three outlier samples (Figures S8 and S9 in Supporting Information S1).

We next consider the relationships on a sample-by-sample basis. Relationships with Th show the weakest *p*-values and can be inconclusive given the 95% confidence intervals (correlation coefficient may equal zero, Table S3). When considering U, six of the 45 samples show p-values below 0.05 (arguably statistically suggestive), three of which demonstrate a p-value below 0.005 (arguably statistically significant) in Table S3. Throughout these relationships, there is inconsistency in the direction (positive vs. negative) of the correlations. Therefore, we consider there to be insufficient evidence of an effect on zircon 2D area and roundness by U content.

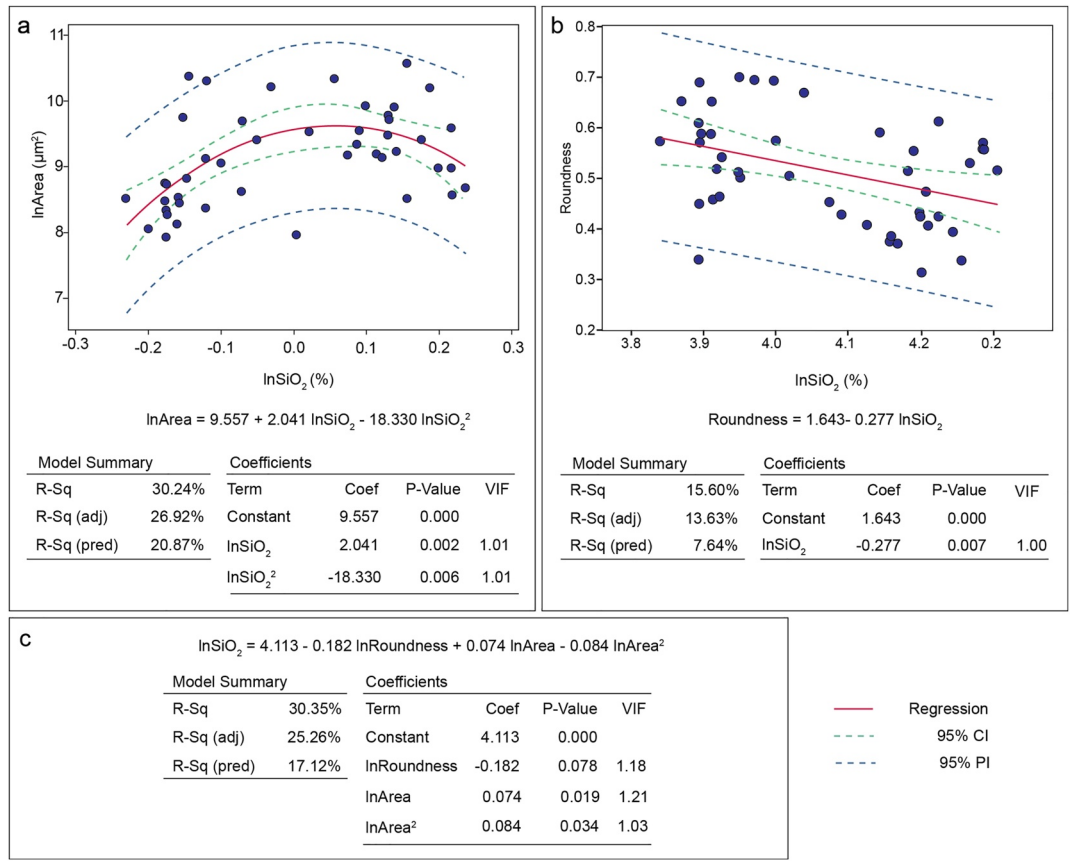

Figure 5. Linear regression models of zircon shape parameters and whole-rock composition, at the sample level. CI denotes Confidence Interval. PI denotes Prediction Interval. VIF designates variance inflation factor. VIF is consistently low, indicating multicollinearity is not a major concern in the models. Model residual plots are provided in Figure S11 in Supporting Information S1. (a) Median sample zircon area vs. whole-rock SiO_2. SiO_2 values were centered by subtracting the mean. A natural logarithm transform is applied to both area and SiO_2. (b) Median sample zircon roundness vs. SiO_2. A natural logarithm transform is applied to SiO_2. We note that a quadratic model for sample median roundness vs. whole-rock SiO_2 performs similarly to the linear model, on our data set. (c) Multiple linear regression model relating median sample zircon area and roundness to whole-rock SiO_2. No biplot is presented for a multivariant relationship. A natural logarithm transform is applied to all variables. Area values were centered by subtracting the mean.

Table S3 demonstrates that the magnitude of the Th/U ratio is not consistently correlated with the magnitude of zircon roundness in our data set. However, increased standard deviation in roundness is associated with increased standard deviation in Th/U ratios of zircon in mafic rocks (Figure 4). This correlation is absent for higher silica rocks.

3.2. Linear Regression

Ordinary Least Squares linear regression was used to model the relationship of median zircon area and roundness versus whole-rock composition, at the sample level (45 samples). The term "linear regression" refers to the linear combination of coefficients and independent variables (Olive, 2017). Linear regression is thus not limited to straight-line relationships of the form $y = mx + c$ and includes quadratic relationships as presented here.

We model sample median area and roundness versus SiO_2 as a proxy for rock type, that is mafic, intermediate, felsic (Figure 5). In addition, the relationships between sample rock grainsize and zircon median area and median roundness were investigated. Grainsize here refers to the upper limit of the most prevalent mineral phase, as reported in the GSWA geochronology reports (GSWA, 2019). Grainsize was neither a strong predictor of median area nor median roundness (Figure S10 in Supporting Information S1) and was omitted from further modeling.

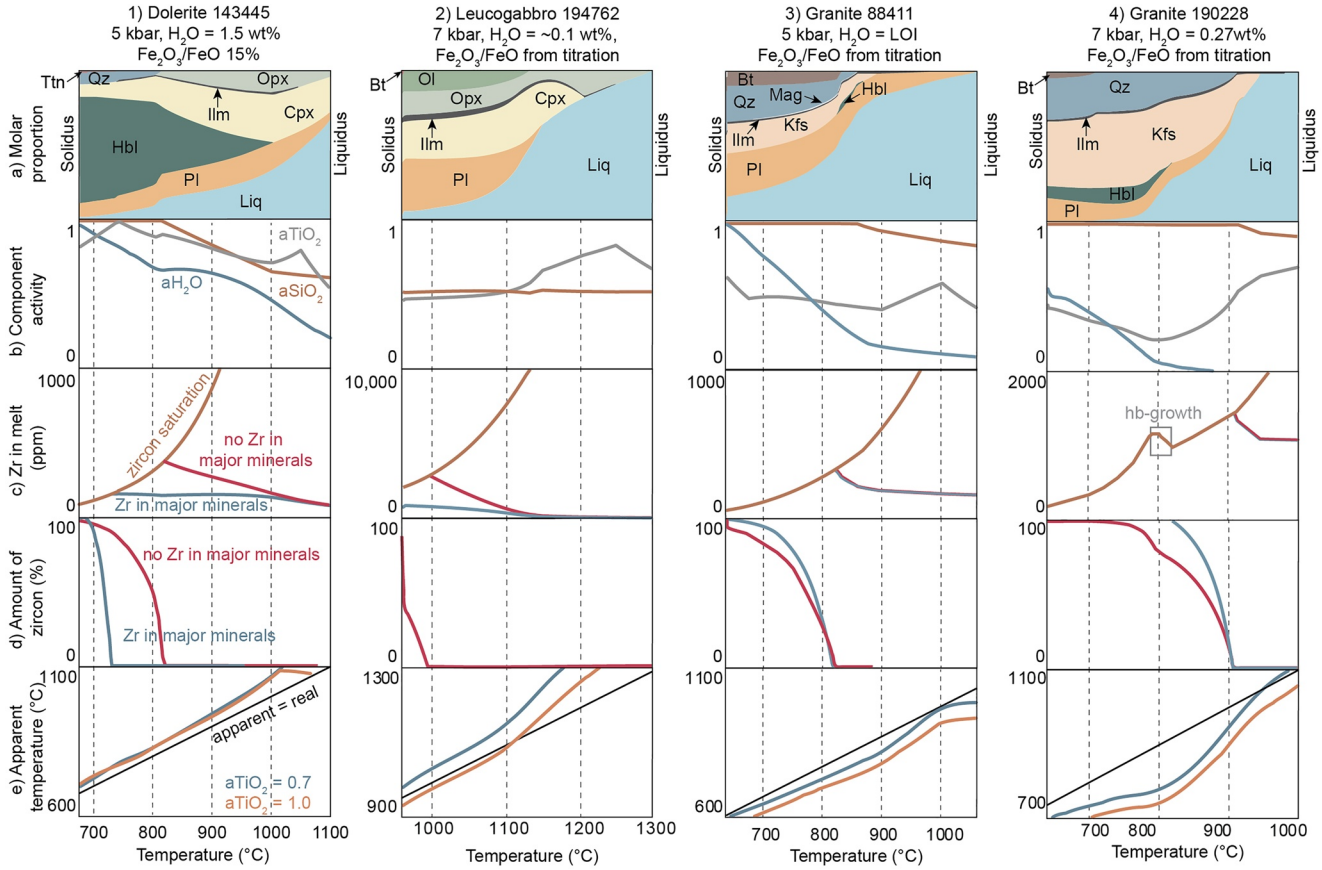

Figure 6. Magmatic crystallization modeling results used to compare zircon and associated mineral phase crystallization in felsic (88411, 190228) and mafic (143445, 194762) samples. Samples 88411 and 143445 are representative of the median zircon shape parameters for the felsic and mafic data sets, respectively. Samples 190228 and 194762 are representative of high temperature, dry felsic and mafic melts respectively, and are coupled with Tescan integrated mineral analyzer-derived mineral maps. Mineral abbreviations after Warr (2021): Qz—quartz, Ilm—ilmenite, Mag—magnetite, Ttn—sphene, Opx—orthopyroxene, Cpx—clinopyroxene, Hbl—hornblende, Pl—plagioclase feldspar, Kfs—potassium feldspar, Ol—olivine, Bt—biotite, Liq—liquid.

Regression models indicate that whole-rock SiO_2 can account for up to ~27% and ~14% of the variability in median zircon area and roundness, respectively (Figures 5a and 5b). When using both median zircon area and roundness to model SiO_2, ~25% of the whole-rock SiO_2 variability in the data set is accounted for (Figure 5c).

3.3. Phase Equilibrium Models

Phase equilibrium models of felsic magmatic rock predict that zircon crystallization begins early in the cooling history and continues until complete crystallization of the melt at solidus (Figure 6). Sufficient Zr and SiO_2 exist for zircon saturation to occur even under the end-member assumption of Zr partitioning into major minerals (Figure 6, models 3 and 4, rows c and d). Results of phase equilibrium modeling of samples 143445 and 194762 demonstrate that mafic melts have a relatively larger cooling interval before reaching zircon supersaturation, in comparison to felsic melts (Figure 6, models 1 and 2, rows c and d). Additionally, the abundance of zircon in the mafic samples is strongly affected by the assumption of Zr partitioning into major minerals.

3.4. TIMA Mineral Maps and BSE Images

We assess zircon growth textures using BSE images and TIMA mineral maps. The relationships discussed here are considered relevant to the hand-picked zircons in GSWA mounts, given the grainsize overlap between the modeled crystal size distributions of TIMA zircon and the measured crystal size distributions of hand-picked zircon (Figure S12 in Supporting Information S1). Given the lower-limits imposed on zircon size by SHRIMP analysis (Nelson, 1997) and the size bias conferred by hand-picking of zircon grains (Zutterkirch et al., 2021), the zircon

10.1029/2023GC011018

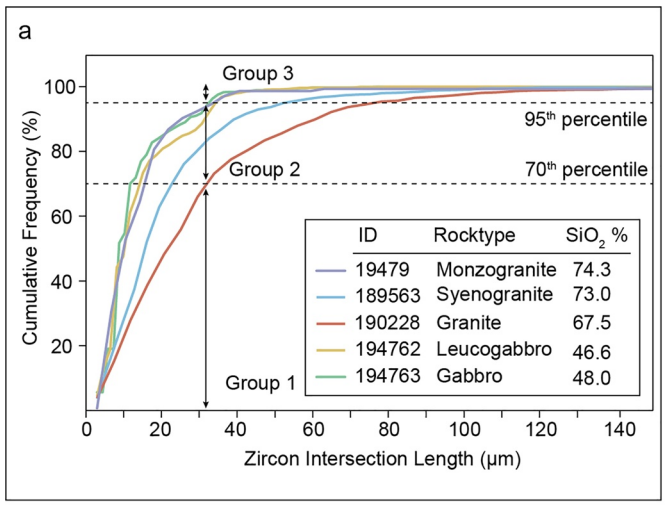

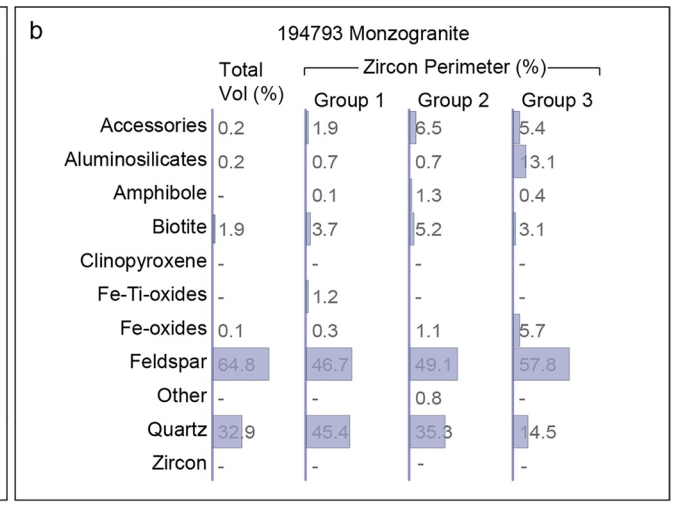

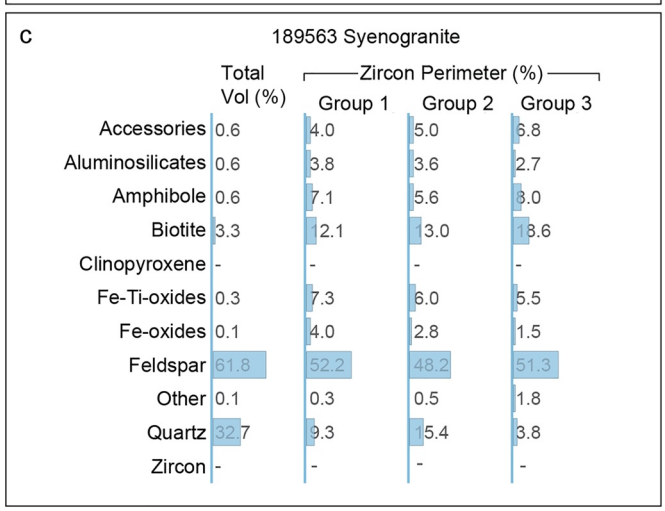

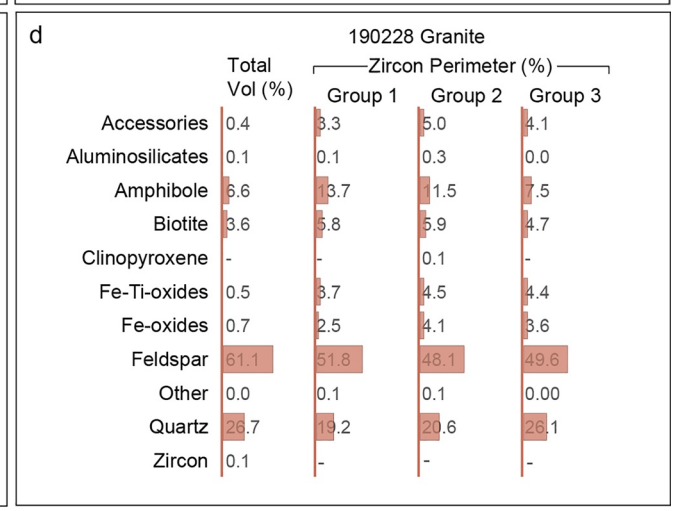

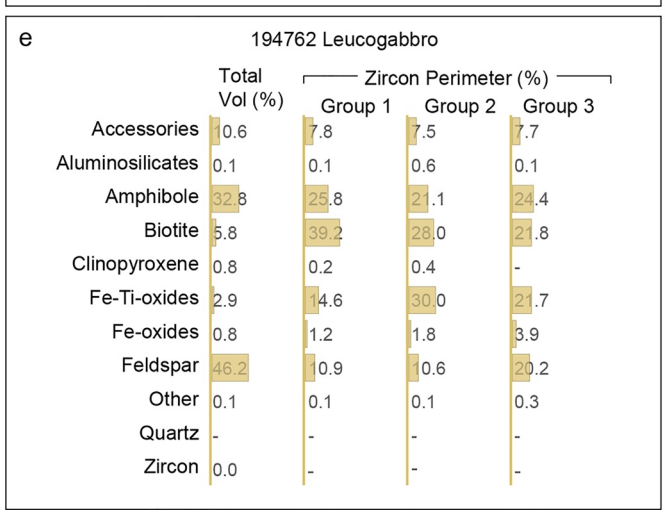

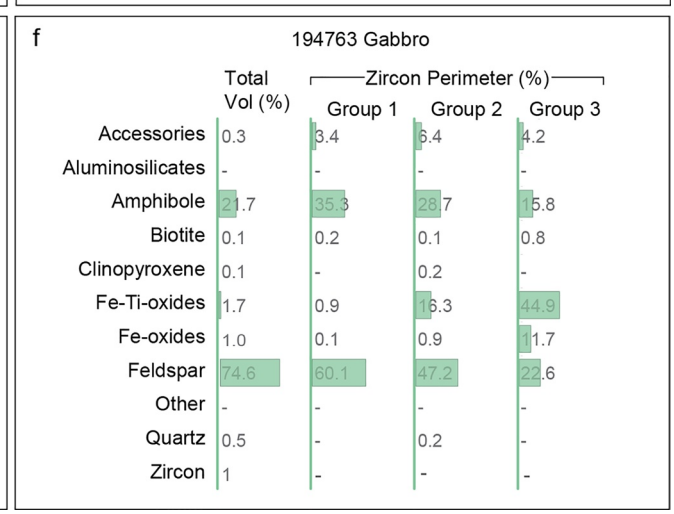

Figure 7.

mounts tend to incorporate an increased proportion of larger zircon than is modeled to exist in the rock billets. Nevertheless, there is significant overlap in the size of zircon seen in the billets with those in the hand-picked mounts. Specifically, an overlap in long axis and short axis distributions of up to 99% is seen in felsic samples, and up to 66% in mafic samples. The reduced overlap in mafic samples may indicate an increased susceptibility to size bias conferred by hand-picking of zircon grains given the generally smaller size of mafic zircon (Figure 5).

Relative changes in the association of certain mineral phases with zircon crystals of different sizes were assessed by comparing the TIMA-derived volume percent of minerals for each billet, to the zircon perimeter percent occupied by mineral phases (Figure 7). Iron-titanium oxides show a strong association with zircon, with the perimeter percent frequently an order of magnitude higher than the volume percent in the sample. In highly felsic rock, the perimeter percent of iron-titanium oxides is highest in the 1st–70th percentile size group (Figures 7b and 7c), which is most representative of the smaller zircon crystals in the samples. This trend reverses as whole-rock silica content drops, such that iron titanium oxides occupy up to 45% of the perimeter around the zircon intersections of the 95–100th percentile size group of mafic samples (Figures 7e and 7f). Oxides similarly display a perimeter percent an order of magnitude larger than the sample volume percent, although they exhibit far lower perimeter percentages than iron-titanium oxides. Major rock forming minerals quartz, feldspar, amphibole and biotite occupy high zircon perimeter percentages in accordance with their high volume percent within the billets. Biotite shows an increasing association with smaller zircon in the dry mafic sample 194762 (Figure 7e). A similar trend is seen with amphibole in mafic sample 194763 (Figure 7f). Sample 194763 (Figure 7f) has virtually no biotite in comparison to 194762 (Figure 7e).

TIMA-derived BSE images provide insight into the textural relationship between zircon and surrounding mineral phases (Figure 8). In highly felsic samples 194793 and 189563, zircon occurs as small, subhedral to euhedral inclusions in, or near the margins of, quartz and feldspar (Figures 8b and 8c). One occurrence of unusually large, recrystallized zircon, which may be hydrothermal in nature, was found in 194793 (Figure 8a). Anhedral to subhedral zircon can also be found between silicate minerals, growing adjacent to or impinging on the boundaries of oxide and iron-titanium oxides (Figure 8d). Granitic sample 190228 shows large, elongated, euhedral zircon growing along silicate mineral boundaries (Figure 8e) and occasionally between hydrous silicates and iron-titanium oxides (Figure 8f). Mafic samples 194762 and 194763 show zircon as rounded, anhedral to subhedral grains growing interstitially alongside accessory minerals (Figure 8h), as "hats" and ribbons on ilmenite (Figure 8i) or as inclusions in ilmenite or oxides (Figure 8j). Rare occurrences of irregular zircon entirely enclosed in felsic minerals may represent remnants of partially melted xenocrysts (Figure 8g).

4. Discussion

4.1. Linear Models of Zircon Shape Versus Geochemistry

There is weak to no correlation between sample median zircon 2D shape and the whole-rock concentrations of trace elements known to preferentially partition into the zircon crystal lattice (Figure 3). In the case of U and Th, this lack of correlation persists at the grain level (Figures S8 and S9 in Supporting Information S1) and suggests that these trace elements have little effect on zircon 2D boundary shape. This does not necessarily negate previous work investigating the controls of crystal face development, as crystal face information is not directly captured in the zircon 2D boundary images (Figure S1 in Supporting Information S1). For trace elements other than U and Th, zircon trace element composition is required to confirm their (lack of) correlation to zircon area and roundness.

The whole-rock chemical parameters that demonstrate the strongest correlations with zircon boundary shape are primarily elements not typically incorporated into the zircon crystal lattice (Figure 3). The nature of the correlations with mafic and felsic melt components are consistently opposed, suggesting that the nature of the melt (mafic

Figure 7. (a) Cumulative frequency plots of zircon intersection lengths (long axes of zircon grains imaged with Tescan integrated mineral analyzer (TIMA)), showing the selected inflection points at approximately 70th and 95th percentiles. Zircon intersections seen in TIMA data are randomly orientated through zircon crystals; thus, these lengths present reduced zircon lengths. The sample's smallest zircon are contained in the 1st–70th percentile group, the 95–100th percentile group is most representative of the largest zircon, and the 70–95th percentile group provides a mix of intersections with zircon of various sizes excluding the smallest. The size of zircon in each percentile group will differ between the samples. (b–f) Bar charts of sample mineral assemblage expressed in volume % (left-most chart), alongside percentage of the zircon perimeter occupied by each mineral, within each of the percentile groups 1–3. In mafic samples (e and f) iron-titanium oxides occupy a large percentage of zircon perimeter relative to their total volume percent in the sample, with perimeter percentage increasing from group 1 to 3. In dry mafic sample 194762 (e), the perimeter percentage of biotite increases from group 3 to group 1. A similar trend is seen with amphibole in mafic sample 194763 (f), which contains virtually no biotite. Iron oxides display a perimeter percentage that is often an order of magnitude larger than their volume percent in the sample in all samples (b–f). Dominant rock forming minerals show little change between volume percent and perimeter percentage across groups 1–3 in all samples (b–f).

10.1029/2023GC011018

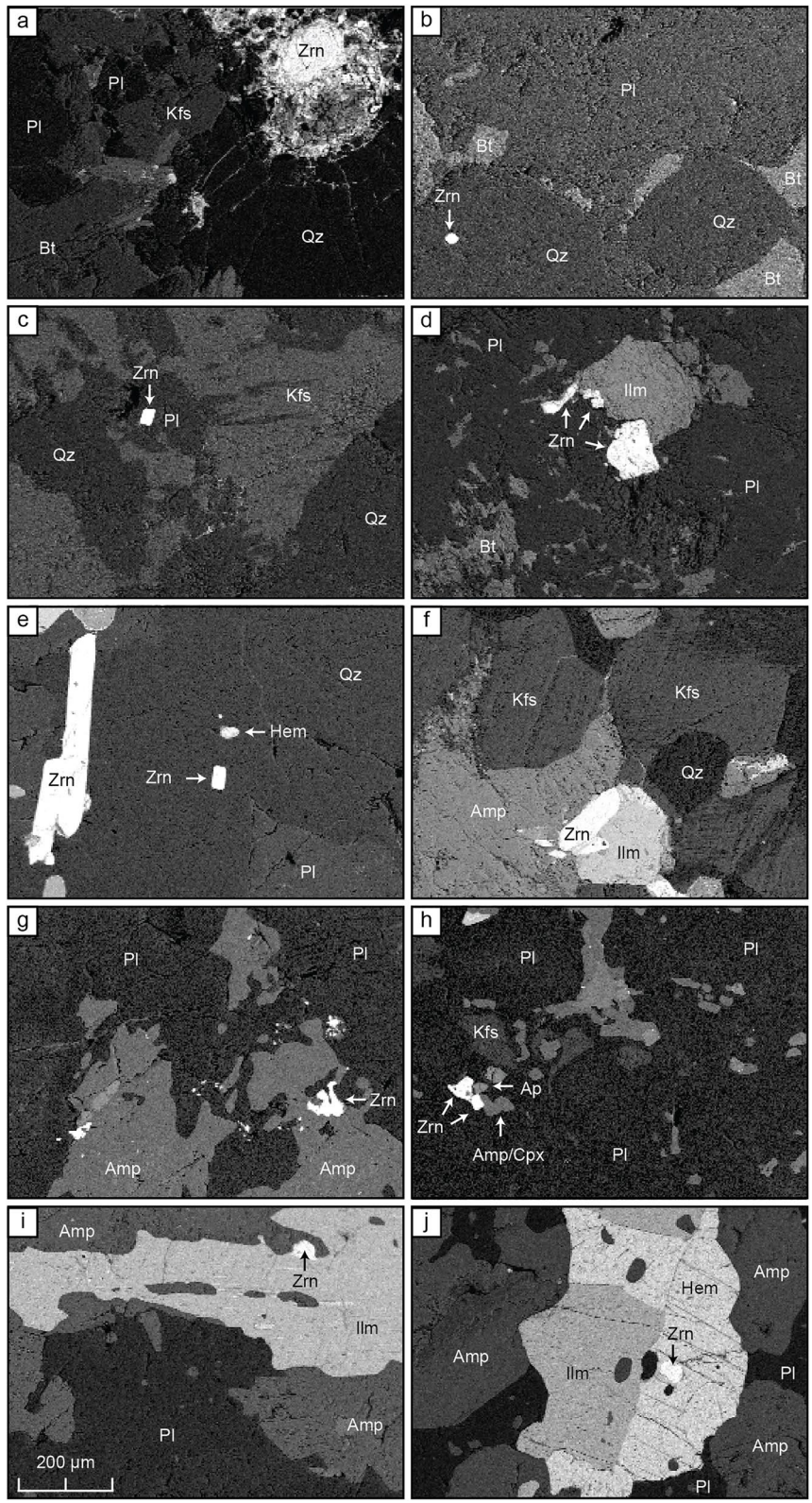

Figure 8.

vs. felsic) influences 2D zircon boundary shape measured at the sample level. Based on the information we have compiled, our results suggest that zircon shape is strongly impacted by factors extrinsic to the crystal lattice.

Median zircon 2D shape, calculated across the data set at 5% whole-rock silica intervals, shows strong (R^2 > 80%) relationships with whole-rock silica (Figure 2). Detailed linear regression models demonstrate that whole-rock composition has a significant, quantifiable relationship to median magmatic zircon grain shape at the sample level, with sample median zircon area and roundness accounting for ~25% (Figure 5c) of whole-rock silica variability in our data set. However, the predictive capability of the relationship via linear regression models is diminished by the unsurprising high natural variance within the geological data set. The linear models are thus explanatory, not predictive.

4.2. Whole-Rock Mineral Assemblage and Competition for Zr

The linear model of zircon shape to whole-rock silica is quadratic in nature, with low silica (<55%) and very high silica (>70%) rocks yielding similarly smaller and more rounded zircon (Figures 2 and 5). At first glance, the whole-rock Zr content shows little (roundness) to no (area) statistically significant relationship with median zircon shape at the sample level (Figure 3, Table S2 in Supporting Information S1). The mafic and highly felsic samples have only slightly lower whole-rock Zr than the intermediate to felsic samples that yield large and elongate zircon (Figure S13 in Supporting Information S1). However, phase equilibrium models show that mafic minerals such as ilmenite, pyroxene, and amphibole will crystallize prior to zircon (Figure 6, models 1 and 2, row a). These minerals are capable of taking in relatively large amounts of Zr (Bea et al., 2006; Fraser et al., 1997), thus further reducing Zr freely available in mafic melt for zircon crystallization, impacting both the amount and size of zircon (Bea et al., 2006). The competition for mineral constituents and resultant suppression of crystallization is conceptually similar to that proposed to act between clinopyroxene and amphibole in mafic-intermediate magmas (Shea & Hammer, 2013). This capture of Zr may account for the weak correlation between whole-rock Zr content and zircon median area and roundness (Figure 3). The strong positive correlation between whole-rock CaO and roundness (Figure 3; Figure S7 and Table S2 in Supporting Information S1) may be due to the presence of pyroxene and amphibole, which increase with decreasing whole-rock silica.

4.3. Zircon Crystallization Timing and Growth Space

In addition to competition for zirconium, both the physical space and time available for zircon crystallization may vary in melts of different silica contents, which could contribute to zircon 2D shape differences. The early onset of zircon crystallization in felsic melts implies a proportion of growth in spatially unconstrained melt and over a protracted period (Figure 6). Mafic melts experienced a delayed onset of zircon crystallization, relative to felsic melts (Figure 6). Conceivably, magmatic zircon derived from cooling of a mafic magma will have a shorter zircon growth interval and a more physically constrained crystal growth environment.

4.4. Localized Zircon Saturation in Mafic Rocks

Recent modeling of zircon crystallization in mafic magmas has proposed that isolated pockets of melt in a cumulate can potentially develop locally Zr-saturated conditions, thus promoting syn-magmatic zircon crystallization in a confined space (Bea et al., 2022). We report a positive correlation between the standard deviation of zircon roundness and the standard deviation of zircon Th/U per sample, a relationship that is present only in the mafic samples (Figure 4). The Th/U ratio of zircon has been posited as an indicator of magmatic fractionation conditions (Kirkland et al., 2015). The lack of relationship between U, Th and zircon area and roundness at the grain level (Table S3) suggests that there is a distinct petrological process extrinsic to zircons

Figure 8. Back-scattered electron images, obtained from Tescan integrated mineral analyzer (TIMA) analysis, showing examples of growth relationships between zircon and adjacent mineral phase. Mineral abbreviations after Warr (2021): Amp—amphibole, Ap—apatite, Bt—biotite, Cpx—clinopyroxene, Hem—hematite, Ilm—ilmenite, Kfs—potassium feldspar, Pl—plagioclase, Qz—quartz, Zrn—zircon. Note that the TIMA classifier is not able to reliably separate amphibole and pyroxene phases in these samples. The scale provided in panel i is applicable to all images. (a) 194793 monzogranite: single occurrence of unusually large, potentially hydrothermal zircon. (b) 194793 monzogranite: zircon enclosed in quartz. (c) 189563 syenogranite: zircon in plagioclase. (d) 189563 syenogranite: zircon growth adjacent to and impinging on iron-titanium oxide. (e) 190228 granite: large, elongate zircon entirely enclosed in felsic minerals. (f) 190228 granite: zircon growth between iron-titanium oxide and amphibole. (g) 194762 leucogabbro: rare occurrence of irregular zircon surrounded by felsic minerals, potentially partially consumed xenocrysts. (h) 194762 leucogabbro: zircon growth interstitially, alongside apatite and either amphibole and/or clinopyroxene. (i) 194763 gabbro: zircon "hat" on iron-titanium oxide. (j) 194763 gabbro: zircon inclusion in iron-oxide.

that promotes increased variability in both zircon Th/U ratios and roundness in mafic rocks. Isolated and variably differentiated melt pockets (Bea et al., 2022) thus appear important for zircon crystallization in low silica melts.

There is a strong association between oxides and zircon (Figures 7, Figure 8). A growth association between zircon and Fe-Ti oxides has previously been identified in mafic igneous rocks (Charlier et al., 2007; Morisset & Scoates, 2008) and a wide range of metamorphic rocks (Austrheim et al., 2008; Bingen et al., 2001; Kovaleva et al., 2017; Rasmussen, 2005). Several authors have described a range of zircon textures (Bingen et al., 2001; Charlier et al., 2007; Kovaleva et al., 2017), including zircon "hats" and corona on Fe-Ti oxides, as also seen in this study (Figure 8). Regardless of the sample, zircon has a higher association with oxides than might be expected for the low volume percent of oxides in the samples. Phase equilibrium models predict continuous co-crystallization of zircon and iron-titanium oxides in both felsic and mafic melts (Figure 6). The trend of increasing Fe-Ti oxides association with smaller zircon in felsic samples, and the inverse in mafic samples (Figure 7), is thus not explained by the crystallization sequence.

The persistent association of zircon with oxides may result from reduced solubility of zircon in a chemically differentiated zone that defines the liquid/crystal interface of the oxides (Bacon, 1989). Silicon is excluded from the growing oxides, producing a Si-enriched "boundary layer." The increased Si concentration reduces zircon solubility (Boehnke et al., 2013; Watson & Harrison, 1983), promoting zircon nucleation on or near the oxide (Bacon, 1989). Figure 8f and 8j demonstrate zircon nucleated on and adjacent to ilmenite and enclosed in amphibole. Additionally, if the crystal/melt partition coefficient for Zr is less than one, Zr is preferentially excluded from the oxide. Slow diffusion of Zr in the locally differentiated boundary layer aids the enrichment of Zr (Bacon, 1989; Green & Watson, 1982) and nucleation of zircon in a spatially constrained zone adjacent to the oxides.

The phenomenon of localized melt differentiation in a mineral boundary layer is most pronounced adjacent to Fe-Ti oxides, but is also linked to ferromagnesian silicates (Bacon, 1989). Figure 8h demonstrates zircon growth adjacent to ferromagnesian silicates and in the absence of oxides. In the case of pyroxene and amphibole, local depletion of Ca, K and Na through their uptake into the silicate crystal lattice could conceivably further reduce zircon solubility, which is characterized by $M = (Na + K + 2Ca)/(Al \times Si)$ (Boehnke et al., 2013). However, Bea et al. (2022) modeled that the presence of crystallizing amphibole will likely prevent zircon crystallization in localized melt pockets if the overall Zr-content of the melt is not higher than ~100 ppm. Nonetheless, many of our mafic samples have whole-rock Zr contents above 100 ppm (Figure S13 in Supporting Information S1).

The boundary layer model assumes minimal melt convection, which would otherwise disrupt the boundary layer (Bacon, 1989), although this is of less concern in mafic cumulates (Bea et al., 2022). In the models of both Bacon (1989) and Bea et al. (2022), material transfer must occur primarily through diffusion, which is slow in silicate melts. However, a small percentage of H_2O (<2%) would increase both zircon solubility (Watson & Harrison, 1983) and Zr diffusion rates by depolymerizing the melt (Bacon, 1989; Stolper, 1982), facilitating elemental transfer, promoting zircon crystallization in ostensibly dry, mafic melts. The phase equilibrium model for sample 194762 (~0.1 wt% H_2O) indicates a low probability of zircon crystallization (Figure 6, model 2) yet this leucogabbro hosts rounded to euhedral igneous zircon (Data Set S1). TIMA results for sample 194762 show that zircon crystals are frequently located along the boundary of Fe-Ti oxides and hydrous silicate phases such as biotite and amphibole (Figure 7).

The "boundary layer" model is limited by its dependence on rapid phenocryst crystallization rates, which might not be realistic in plutonic rocks (Bacon, 1989). This model is thus unlikely to be solely responsible for the association between zircon and oxides seen in our samples. In mafic igneous rocks, zircon growth has also been attributed to exsolution of Zr from ilmenite during subsolidus cooling (Charlier et al., 2007; Morisset & Scoates, 2008). Exsolved Zr is thought to react with SiO_2 scavenged from the adjacent silicate minerals or ilmenite itself to produce zircon (Charlier et al., 2007; Morisset & Scoates, 2008). This crystallization process may also contribute to zircon's strong affinity for Fe-Ti oxides in our mafic samples (Figure 7). Figure 8i demonstrates a potential exsolution feature of a zircon "hat" on ilmenite. Both the boundary layer and exsolution models facilitate the late-stage growth of zircon in low silica melts, under localized disequilibrium conditions that promote zircon nucleation.

The crystallization of zircon in mafic rocks, as predicted by the phase equilibrium models, occurs in at least two configurations: (a) crystallization of zircon in isolated regions of melt where sufficient elements for zircon growth have accumulated, potentially under disequilibrium conditions promoted by a boundary layer effect and localized melt differentiation and (b) derivation of Zr and SiO_2 from Fe-Ti oxides and surrounding silicate minerals upon cooling of the melt. These two growth occurrence models are consistent with observations reported by Morisset and Scoates (2008) and inferred by Charlier et al. (2007). Hence, the tendency toward smaller zircon size in mafic rocks is likely imposed by (a) the physically constrained interstitial spaces and predominantly oxide and Fe-Ti-oxide induced boundary layers (Figure 8), (b) shorter crystallization time (Figure 6), (c) the greater incorporation of Zr into mafic minerals (Bea et al., 2006; Fraser et al., 1997) which reduces the amount of Zr available for zircon crystallization, and potentially (d) the reduced availability of SiO_2 which creates a greater dependence of zircon saturation on localized pockets of differentiated melt (Bea et al., 2022).

4.5. Zircon in Highly Differentiated Melt

Smaller and potentially more rounded zircon are also seen in our samples with whole-rock silica above ~70% (Figures 2 and 5). "Rounded and irregular" zircons in felsic rocks have previously been speculated to derive from "late differentiates" (Poldervaart, 1956), which agrees with our observations. A slight decrease in whole-rock Zr attends samples with silica contents above ~70% (Figure S13 in Supporting Information S1), which may inhibit zircon growth. Increasing whole-rock silica implies increasingly differentiated parent melts that, in addition to increased silica, likely carry increased volatiles. Delayed zircon crystallization in highly felsic melts has been attributed to increased water content (Kirkland et al., 2021), providing a possible mechanism for the zircon shape trend reversals we see in our high silica samples. These late differentiates would experience reduced crystallization time and growth space, like zircon in mafic melts. We note also that increased melt viscosity in granitic melts, with increased volatile content, has previously been used to account for reduced zircon length (Kostov, 1973).

5. Conclusions

This work provides a conceptual framework to model the controls of magmatic zircon 2D shape. Forty-five mafic to felsic samples from igneous rock, broadly representative of both Archean and Proterozoic crust, demonstrate that whole-rock composition exerts a significant influence on magmatic zircon grain shape. Multiple linear regression, using sample median zircon crystal area and roundness, can account for just over a quarter of the variance in whole-rock silica content across the data set investigated. Statistically significant ($p < 0.01$) relationships indicate that populations of zircon crystals tend toward increased area and reduced roundness as melts become more siliceous; however, this trend reverses at high silica contents (>65%).

Sample median zircon area and roundness show strong correlations with elements not typically incorporated into the zircon crystal lattice, suggesting that factors extrinsic to the zircon crystal may exert significant control on the zircon boundary shape. This finding does not contradict previous works relating the development of zircon prisms and pyramids to chemical conditions. Rather, it suggests that these links are not discernible in the type of shape measurements considered here nor in measurements collected most readily as part of standard zircon geochronological and geochemical analyses.

Results of phase equilibrium modeling of mafic and felsic samples, in conjunction with TIMA mineral maps, indicate that the predisposition of zircon shape may be strongly influenced by the fundamentally different growth environments in mafic vs. felsic melts, consistent with modeling results of previous authors. Zircon crystallization in felsic melts begins early in the crystallization history in spatially unconstrained melt and continues for a protracted period. Conversely, zircon crystallization in a mafic melt begins late in the crystallization history at which point (a) Zr in the melt may be largely reduced due to its incorporation in earlier-crystallized pyroxenes and amphiboles, (b) growth likely occurs in spatially constrained interstitial spaces, and (c) growth occurs over a short period. Mafic zircon growth may also initiate earlier in the crystallization sequence, in locally differentiated melt pockets that are physically constrained.

Disequilibrium growth processes plays a dominant role in mafic zircon crystallization, with the potential for zircon crystallization being strongly influenced by the local diffusion of Zr and SiO_2. Under these conditions, mafic zircon crystallization may have a greater tendency to initiate from the exsolution of Zr from Ti-Fe oxides, or in the physically constrained and chemically differentiated boundary layers of Ti-Fe oxides in particular but also Fe-oxides.

Conflict of Interest

The authors declare no conflicts of interest relevant to this study.

Data Availability Statement

Data were obtained from the GSWA's public repository of geochronology (DMIRS, 2022b) and geochemistry (DMIRS, 2022a), and the 2019 Geochronology Compilation (GSWA, 2019). Data for Proterozoic crustal composition comprises Navdat, Georoc, and USGS entries freely downloaded from EarthChem (2021) and Keller et al. (2015). Data for Archean crustal composition was similarly sourced from EarthChem as per Keller et al. (2015), as well as plutonic, pegmatitic, volcanic and meta-igneous samples from the Supporting Information of Tang et al. (2016). Data used to construct Figure S1 in Supporting Information S1 are published in Pupin and Turco (1972) and Pupin (1980). Zircon images are available in GSWA (2019) and can also be requested directly from the GSWA. Shape measurements were made using AnalyZr (Scharf et al., 2022). AnalyZr is available as open-source software under the MIT license via GitHub (Scharf & Daggitt, 2023). The zircon shape-composition data set used for linear regression modelling is provided as Data Set S1 and online at Dryad (Scharf et al., 2023). Clustering algorithms and correlation matrices were created using SPSS 27 (IBM Corp., 2020), which requires a subscription for use. Linear regression modelling was carried out in Minitab 21.1 (Minitab, Inc., 2022), which requires a subscription for use. Crystal size distributions were created using ShapeCalc, which may be accessed in the Supporting Information of Mangler et al. (2022), and CSDCorrections, which may be accessed through software links provided in Higgins (2000). The "M" parameter was calculated using the GCDkit plugin for RStudio (Janoušek et al., 2006), which may be freely downloaded (https://www.gcdkit.org/download).

Acknowledgments
This project was funded through Minerals Research Institute of Western Australia (MRIWA) Grant M551 in collaboration with Iluka Resources and Curtin University. The first author was funded by the Australian Government Research Training Program Stipend Scholarship. We thank the Geological Survey of Western Australia for providing extensive data sets for this work. Dr. Alex Walker of Curtin University is thanked for his insight into TIMA analysis. Open access publishing facilitated by Curtin University, as part of the Wiley - Curtin University agreement via the Council of Australian University Librarians.

References

Aitchison, J. C., Cluzel, D., Ireland, T. R., Zhou, R., Lian, D., Patias, D., et al. (2022). Solid-phase transfer into the forearc mantle wedge: Rutile and zircon xenocrysts fingerprint subducting sources. *Earth and Planetary Science Letters*, *577*, 117251. https://doi.org/10.1016/j.epsl.2021.117251

Austrheim, H., Putnis, C. V., Engvik, A. K., & Putnis, A. (2008). Zircon coronas around Fe-Ti oxides: A physical reference frame for metamorphic and metasomatic reactions. *Contributions to Mineralogy and Petrology*, *156*(4), 517–527. https://doi.org/10.1007/s00410-008-0299-8

Bacon, C. R. (1989). Crystallization of accessory phases in magmas by local saturation adjacent to phenocrysts. *Geochimica et Cosmochimica Acta*, *53*(5), 1055–1066. https://doi.org/10.1016/0016-7037(89)90210-X

Bea, F., Bortnikov, N., Cambeses, A., Chakraborty, S., Molina, J. F., Montero, P., et al. (2022). Zircon crystallization in low-Zr mafic magmas: Possible or impossible? *Chemical Geology*, *602*, 120898. https://doi.org/10.1016/j.chemgeo.2022.120898

Bea, F., Montero, P., & Ortega, M. (2006). A LA-ICP-MS evaluation of Zr reservoirs in common crustal rocks: Implications for Zr and Hf geochemistry, and zircon-forming processes. *The Canadian Mineralogist*, *44*(3), 693–714. https://doi.org/10.2113/gscanmin.44.3.693

Belousova, E. A., Griffin, W. L., O'Reilly, S. Y., & Fisher, N. I. (2002). Igneous zircon: Trace element composition as an indicator of source rock type. *Contributions to Mineralogy and Petrology*, *143*(5), 602–622. https://doi.org/10.1007/s00410-002-0364-7

Benisek, A., & Finger, F. (1993). Factors controlling the development of prism faces in granite zircons: A microprobe study. *Contributions to Mineralogy and Petrology*, *114*(4), 441–451. https://doi.org/10.1007/BF00321749

Benjamin, D. J., & Berger, J. O. (2019). Three recommendations for improving the use of *p*-values. *The American Statistician*, *73*(1), 186–191. https://doi.org/10.1080/00031305.2018.1543135

Benjamin, D. J., Berger, J. O., Johannesson, M., Nosek, B. A., Wagenmakers, E. J., Berk, R., et al. (2018). Redefine statistical significance. *Nature Human Behaviour*, *2*(1), 6–10. https://doi.org/10.1038/s41562-017-0189-z

Bingen, B., Austrheim, H., & Whitehouse, M. (2001). Ilmenite as a source for zirconium during high-grade metamorphism? Textural evidence from the caledonides of Western Norway and implications for zircon geochronology. *Journal of Petrology*, *42*(2), 355–375. https://doi.org/10.1093/petrology/42.2.355

Boehnke, P., Watson, E. B., Trail, D., Harrison, T. M., & Schmitt, A. K. (2013). Zircon saturation re-revisited. *Chemical Geology*, *351*, 324–334. https://doi.org/10.1016/j.chemgeo.2013.05.028

Cambeses, A., Chakraborty, S., Jöns, N., Montero, P., & Bea, F. (2023). How does inherited zircon survive in partially molten mantle: Insights on modes of magma transport in the mantle from nanoscale melt-crystal interaction experiments. *Earth and Planetary Science Letters*, *601*, 117911. https://doi.org/10.1016/j.epsl.2022.117911

Cashman, K. V., & Marsh, B. D. (1988). Crystal size distribution (CSD) in rocks and the kinetics and dynamics of crystallization II: Makaopuhi Lava Lake. *Contributions to Mineralogy and Petrology*, *99*(3), 292–305. https://doi.org/10.1007/BF00375363

Charlier, B., Skår, Ø., Korneliussen, A., Duchesne, J. C., & Vander Auwera, J. (2007). Ilmenite composition in the Tellnes Fe-Ti deposit, SW Norway: Fractional crystallization, postcumulus evolution and ilmenite-zircon relation. *Contributions to Mineralogy and Petrology*, *154*(2), 119–134. https://doi.org/10.1007/s00410-007-0186-8

Colquhoun, D. (2014). *An investigation of the false discovery rate and the misinterpretation of p*-values (Vol. 1). Royal Society Open Science. https://doi.org/10.1098/rsos.140216

Corfu, F., Hanchar, J. M., Hoskin, P. W. O., & Kinny, P. (2003). Atlas of zircon textures. *Reviews in Mineralogy and Geochemistry*, *53*(1), 469–500. https://doi.org/10.2113/0530469

DMIRS. (2022a). GeoChem extract [Dataset]. Retrieved from http://geochem.dmp.wa.gov.au/geochem/

DMIRS. (2022b). GeoVIEW [Dataset]. Retrieved from https://geoview.dmp.wa.gov.au/geoview/?Viewer=GeoView

EarthChem (2021). Earth Chem [Dataset]. Retrieved from http://www.earthchem.org/
Erdmann, S., Scaillet, B., & Kellett, D. A. (2010). Xenocryst assimilation and formation of peritectic crystals during magma contamination: An experimental study. *Journal of Volcanology and Geothermal Research*, *198*(3–4), 355–367. https://doi.org/10.1016/j.jvolgeores.2010.10.002
Fraser, G., Ellis, D., & Eggins, S. (1997). Zirconium abundance in granulite-facies minerals, with implications for zircon geochronology in high-grade rocks. *Geology*, *25*(7), 607–610. https://doi.org/10.1130/0091-7613(1997)025<0607:ZAIGFM>2.3.CO;2
Freedman, D., & Diaconis, P. (1981). On the histogram as a density estimator:L2 theory. *Zeitschrift für Wahrscheinlichkeitstheorie und Verwandte Gebiete*, *57*(4), 453–476. https://doi.org/10.1007/BF01025868
Gartmair, G., Barham, M., & Kirkland, C. L. (2023). One size does not fit all: Refining zircon provenance interpretations via integrated grain shape, geochronology, and Hf isotope analysis. *Geoscience Frontiers*, *14*(4), 101579. https://doi.org/10.1016/j.gsf.2023.101579
Green, T. H., & Watson, E. B. (1982). Crystallization of apatite in natural magmas under high pressure, hydrous conditions, with particular reference to "Orogenic" rock series. *Contributions to Mineralogy and Petrology*, *79*(1), 96–105. https://doi.org/10.1007/bf00376966
GSWA. (2019). Compilation of geochronology information, 2019 [Dataset]. Geological Survey of Western Australia. Retrieved from https://dmpbookshop.eruditetechnologies.com.au/product/compilation-of-geochronology-information-2019.do
Hanchar, J. M. (2013). Zircon. In W. Rink, & J. Thompson (Eds.) *Encyclopedia of scientific dating methods*. https://doi.org/10.1007/978-94-007-6326-5_58-1
Hanchar, J. M., & van Westrenen, W. (2007). Rare Earth element behavior in Zircon—Melt systems. *Elements*, *3*(1), 37–42. https://doi.org/10.2113/gselements.3.1.37
Higgins, M. D. (1994). Numerical modeling of crystal shapes in thin sections: Estimation of crystal habit and true size. *American Mineralogist*, *79*, 113–119.
Higgins, M. D. (2000). Measurement of crystal size distributions. *American Mineralogist*, *85*(9), 1105–1116. https://doi.org/10.2138/am-2000-8-901
Hoskin, P. W. O., & Schaltegger, U. (2003). The composition of zircon and igneous and metamorphic petrogenesis. *Reviews in Mineralogy and Geochemistry*, *53*(1), 27–62. https://doi.org/10.2113/0530027
IBM Corp. (2020). IBM SPSS stastics for Windows, version 27.0 [Software]. IBM Corp. Retrieved from www.ibm.com/spss
Janoušek, V., Farrow, C. M., & Erban, V. (2006). Interpretation of whole-rock geochemical data in igneous geochemistry: Introducing Geochemical Data Toolkit (GCDkit). *Journal of Petrology*, *47*(6), 1255–1259. https://doi.org/10.1093/petrology/egl013
Keller, C., Schoene, B., Barboni, M. et al. Volcanic-plutonic parity and the differentiation of the continental crust. *Nature*, *523*, 301–307 (2015). https://doi.org/10.1038/nature14584
Kirkland, C. L., Smithies, R. H., Taylor, R. J. M., Evans, N., & McDonald, B. (2015). Zircon Th/U ratios in magmatic environs. *Lithos*, *212–215*, 397–414. https://doi.org/10.1016/j.lithos.2014.11.021
Kirkland, C. L., Yakymchuk, C., Olierook, H. K. H., Hartnady, M. I. H., Gardiner, N. J., Moyen, J. F., et al. (2021). Theoretical versus empirical secular change in zircon composition. *Earth and Planetary Science Letters*, *554*, 116660. https://doi.org/10.1016/j.epsl.2020.116660
Kostov, I. (1973). Zircon morphology as a crystallogenetic indicator. *Kristall und Technik*, *8*(1–3), 11–19. https://doi.org/10.1002/crat.19730080103
Kovaleva, E., Austrheim, H. O., & Klötzli, U. S. (2017). Interpretation of zircon coronae textures from metapelitic granulites of the Ivrea-Verbano Zone, northern Italy: Two-stage decomposition of Fe-Ti oxides. *Solid Earth*, *8*(4), 789–804. https://doi.org/10.5194/se-8-789-2017
Larsen, L. H., & Poldervaart, A. (1957). Measurement and distribution of zircons in some granitic rocks of magmatic origin. *Mineralogical Magazine and Journal of the Mineralogical Society*, *31*(238), 544–564. https://doi.org/10.1180/minmag.1957.031.238.03
Makuluni, P., Kirkland, C., & Barham, M. (2019). Zircon grain-shape holds provenance information; a case study from southwestern Australia. *Geological Journal*, *54*(3), 1279–1293. https://doi.org/10.1002/gj.3225
Mangler, M. F., Humphreys, M. C. S., Wadsworth, F. B., Iveson, A. A., & Higgins, M. D. (2022). Variation of plagioclase shape with size in intermediate magmas: A window into incipient plagioclase crystallisation. *Contributions to Mineralogy and Petrology*, *177*(6), 1–21. https://doi.org/10.1007/s00410-022-01922-9
Markwitz, V., & Kirkland, C. L. (2018). Source to sink zircon grain shape: Constraints on selective preservation and significance for Western Australian Proterozoic basin provenance. *Geoscience Frontiers*, *9*(2), 415–430. https://doi.org/10.1016/j.gsf.2017.04.004
Marsh, B. D. (1988). Crystal size distribution (CSD) in rocks and the kinetics and dynamics of crystallization—I. Theory. *Contributions to Mineralogy and Petrology*, *99*(3), 277–291. https://doi.org/10.1007/BF00375362
McGovern, A., Lagerquist, R., Gagne, D. J. I., Jergensen, G. E., Elmore, K. L., Homeyer, C. R., & Smith, T. (2019). Making the black box more transparent: Understanding the physical implications of machine learning. *Bulletin of the American Meteorological Society*, *100*(11), 2175–2199. https://doi.org/10.1175/BAMS-D-18-0195.1
Minitab, Inc. (2022). Minitab statistical software version 27.1 [Software]. Minitab, Inc. Retrieved from www.minitab.com
Moecher, D. P., & Samson, S. D. (2006). Differential zircon fertility of source terranes and natural bias in the detrital zircon record: Implications for sedimentary provenance analysis. *Earth and Planetary Science Letters*, *247*(3–4), 252–266. https://doi.org/10.1016/j.epsl.2006.04.035
Morisset, C. E., & Scoates, J. S. (2008). Origin of zircon rims around ilmenite in mafic plutonic rocks of Proterozoic anorthosite suites. *The Canadian Mineralogist*, *46*(2), 289–304. https://doi.org/10.3749/canmin.46.2.289
Nardi, L. V. S., Formoso, M. L. L., Müller, I. F., Fontana, E., Jarvis, K., & Lamarão, C. (2013). Zircon/rock partition coefficients of REEs, Y, Th, U, Nb, and Ta in granitic rocks: Uses for provenance and mineral exploration purposes. *Chemical Geology*, *335*, 1–7. https://doi.org/10.1016/j.chemgeo.2012.10.043
Nelson, D. R. (1997). *Record 1997/2: Compilation of SHRIMP U-Pb zircon geochronology data, 1996*. Western Australia Geological Survey.
Olierook, H. K. H., Kirkland, C. L., Szilas, K., Hollis, J. A., Gardiner, N. J., Steenfelt, A., et al. (2020). Differentiating between inherited and autocrystic zircon in granitoids. *Journal of Petrology*, *61*(8). https://doi.org/10.1093/petrology/egaa081
Olive, D. J. (2017). *Linear regression* (1st ed.). Springer International Publishing. https://doi.org/10.1007/978-3-319-55252-1
Poldervaart, A. (1956). Zircon in rocks 2: Igneous rocks. *American Journal of Science*, *254*(9), 521–544. https://doi.org/10.2475/ajs.254.9.521
Pupin, J., & Turco, G. (1972). Une typologie originale du zircon accessoire. *Bulletin de la Societe Française de Mineralogie et de Cristallographie*, *95*(3), 348–359. https://doi.org/10.3406/bulmi.1972.6688
Pupin, J. P. (1980). Zircon and granite petrology. *Contributions to Mineralogy and Petrology*, *73*(3), 207–220. https://doi.org/10.1007/BF00381441
Rasmussen, B. (2005). Zircon growth in very low grade metasedimentary rocks: Evidence for zirconium mobility at ~250°C. *Contributions to Mineralogy and Petrology*, *150*(2), 146–155. https://doi.org/10.1007/s00410-005-0006-y
Ribbe, H. P. (1982). Orthosilicates. In H. P. Ribbe (Ed.), *Reviews in mineralogy* (pp. 67–112).
Rubatto, D. (2002). Zircon trace element geochemistry: Partitioning with garnet and the link between U-Pb ages and metamorphism. *Chemical Geology*, *184*(1–2), 123–138. https://doi.org/10.1016/S0009-2541(01)00355-2
Scharf, T., & Daggitt, M. L. (2023). AnalyZr: Zircon separation v1.3 (v1.3) [Software]. Zenodo. https://doi.org/10.5281/zenodo.7885059

Scharf, T., Kirkland, C. L., Barham, M., Yukymchuk, C., & Puzyrev, V. (2023). Zircon 2D shape and geochemistry [Dataset]. Dryad. https://doi.org/10.5061/dryad.vmcvdnczt
Scharf, T., Kirkland, C. L., Daggitt, M. L., Barham, M., & Puzyrev, V. (2022). AnalyZr: A Python application for zircon grain image segmentation and shape analysis. *Computers & Geosciences*, *162*, 105057. https://doi.org/10.1016/j.cageo.2022.105057
Schulz, B., Klemd, R., & Brätz, H. (2006). Host rock compositional controls on zircon trace element signatures in metabasites from the Austroalpine basement. *Geochimica et Cosmochimica Acta*, *70*(3), 697–710. https://doi.org/10.1016/j.gca.2005.10.001
Shea, T., & Hammer, J. E. (2013). Kinetics of cooling- and decompression-induced crystallization in hydrous mafic-intermediate magmas. *Journal of Volcanology and Geothermal Research*, *260*, 127–145. https://doi.org/10.1016/j.jvolgeores.2013.04.018
Sitar, M. C., & Leary, R. J. (2022). Technical note: Colab_zirc_dims: A google-Colab-based toolset for automated and semi-automated measurement of mineral grains in LA-ICP-MS images using deep learning models. *Geochronology Discuss* (preprint). https://doi.org/10.5194/gchron-2022-12
Spencer, C. J., Kirkland, C. L., & Taylor, R. J. M. (2016). Strategies towards statistically robust interpretations of in situ U-Pb zircon geochronology. *Geoscience Frontiers*, *7*(4), 581–589. https://doi.org/10.1016/j.gsf.2015.11.006
Stolper, E. (1982). Water in silicate glasses: An infrared spectroscopic study. *Contributions to Mineralogy and Petrology*, *81*, 1–17. https://doi.org/10.1007/BF00371154
Tailby, N. D., Walker, A. M., Berry, A. J., Hermann, J., Evans, K. A., Mavrogenes, J. A., et al. (2011). Ti site occupancy in zircon. *Geochimica et Cosmochimica Acta*, *75*(3), 905–921. https://doi.org/10.1016/j.gca.2010.11.004
Tang, M., Chen, K., & Rudnick, R. L. (2016). Archean upper crust transition from mafic to felsic marks the onset of plate tectonics. *Science*, *351*(6271), 372–375. https://doi.org/10.1126/science.aad5513
Toms, B. A., Barnes, E. A., & Ebert-Uphoff, I. (2020). Physically interpretable neural networks for the geosciences: Applications to Earth system variability. *Journal of Advances in Modeling Earth Systems*, *12*(9), 1–20. https://doi.org/10.1029/2019MS002002
Vavra, G. (1990). On the kinematics of zircon growth and its petrogenetic significance: A cathodoluminescence study. *Contributions to Mineralogy and Petrology*, *106*(1), 90–99. https://doi.org/10.1007/BF00306410
Warr, L. N. (2021). IMA–CNMNC approved mineral symbols. *Mineralogical Magazine*, *85*, 291–320. https://doi.org/10.1180/mgm.2021.43
Watson, E. B., & Harrison, T. M. (1983). Zircon saturation revisited: Temperature and composition effects in a variety of crustal magma types. *Earth and Planetary Science Letters*, *64*(2), 295–304. https://doi.org/10.1016/0012-821X(83)90211-X
Xu, W., Hou, Y., Hung, Y. S., & Zou, Y. (2013). A comparative analysis of Spearmans rho and Kendalls tau in normal and contaminated normal models. *Signal Processing*, *93*(1), 261–276. https://doi.org/10.1016/j.sigpro.2012.08.005
Zeh, A., & Cabral, A. R. (2021). Combining detrital zircon shape and U–Pb–Hf isotope analyses for provenance studies—An example from the Aquiri region, Amazon Craton, Brazil. *Precambrian Research*, *364*, 106343. https://doi.org/10.1016/j.precamres.2021.106343
Zutterkirch, I. C., Kirkland, C. L., Barham, M., & Elders, C. (2021). Thin-section detrital zircon geochronology mitigates bias in provenance investigations. *Journal of the Geological Society*, *179*(2). https://doi.org/10.1144/jgs2021-070

References From the Supporting Information

Abràmoff, M. D., Magalhães, P. J., & Ram, S. J. (2004). Image processing with ImageJ. *Biophotonics International*, *11*, 36–41. https://doi.org/10.1201/9781420005615.ax4
Bédard, J. H. (2006). A catalytic delamination-driven model for coupled genesis of Archaean crust and sub-continental lithospheric mantle. *Geochimica et Cosmochimica Acta*, *70*(5), 1188–1214. https://doi.org/10.1016/j.gca.2005.11.008
Chinga, G. (2002). Shape descriptors. [WWW Document]. Retrieved from https://imagej.nih.gov/ij/plugins/descriptors.html
Goldschmidt, V. M. (1937). The principles of distribution of chemical elements in minerals and rocks. The seventh Hugo Müller Lecture, delivered before the Chemical Society on March 17, 1937. *Journal of the Chemical Society*, *0*(0), 655–673. https://doi.org/10.1039/jr9370000655
Holland, T. J. B., Green, E. C. R., & Powell, R. (2018). Melting of peridotites through to granites: A simple thermodynamic model in the system KNCFMASHTOCr. *Journal of Petrology*, *59*(5), 881–900. https://doi.org/10.1093/petrology/egy048
Holland, T. J. B., & Powell, R. (2011). An improved and extended internally consistent thermodynamic dataset for phases of petrological interest, involving a new equation of state for solids. *Journal of Metamorphic Geology*, *29*(3), 333–383. https://doi.org/10.1111/j.1525-1314.2010.00923.x
Hu, M. (1962). Visual pattern recognition by moment invariants. *IEEE Transactions on Information Theory*, *8*(2), 179–187. https://doi.org/10.4324/9781315714851-8
Nelson, D. R. (1999). *Compilation of geochronology data, 1998*. Geological Survey of Western Australia.
Powell, R., & Holland, T. J. B. (1988). An internally consistent dataset with uncertainties and correlations: 3. Applications to geobarometry, worked examples and a computer program. *Journal of Metamorphic Geology*, *6*(2), 173–204. https://doi.org/10.1111/j.1525-1314.1988.tb00415.x
scikit-image.org. (2021). scikit-image 0.18.0 docs [WWW Document]. Retrieved from https://scikit-image.org/docs/0.18.x/
van der Walt, S., Schönberger, J. L., Nunez-Iglesias, J., Boulogne, F., Warner, J. D., Yager, N., et al. (2014). The scikit-image contributors, 2014. scikit-image: Image processing in Python. *PeerJ*, *2*, e453. https://doi.org/10.7717/peerj.453